Interfacial Exchange Phenomena Driven by Ferromagnetic Domains

José Manuel Díez, José Luis F. Cuñado, Pavel Lapa, Raúl Solís, Icíar Arnay, Patricia Pedraz, Paolo Perna, Alberto Bollero, Rodolfo Miranda, Ivan K. Schuller, and Julio Camarero*

Interfacial proximity effects in antiferromagnetic/ferromagnetic (AFM/FM) bilayers control the exchange-bias (EB) phenomena exploited in most spintronic devices, although still is lack of full understanding. Discordant results, including different exchange-bias field (H_E), coercivity (H_C), or blocking temperature (T_B) found even in similar systems, are usually ascribed to uncontrolled parameters, namely dissimilar interfacial defects, structure, and thicknesses. Here, it is shown in the very same sample that the magnetic domain structure during the magnetization reversal of the FM layer controls those mentioned effects. Simultaneous transport and vectorial-resolved magnetic measurements performed in a V_2O_3/Co system during warming after different field cooling (FC) procedures exhibit a strong dependence on the FC angle and the domain structure of the FM layer. Remarkably, magnetization reversal analysis reveals 35 K of variation in T_B and up to a factor of two in H_E. These observations can be explained within the random-field model for the interfacial exchange coupling with a fixed AFM domain structure in contact with a variable (angle-dependent) FM domain structure. The results highlight the importance of the domain structure and magnetization reversal of the FM layer (not previously considered) in the EB phenomena, with potential to tailor interfacial effects in future spintronic devices.

1. Introduction

The understanding and design of complex multi-layered magnetic nanostructures is one of the active frontiers in nanomagnetism. Dimensionality and interfacial effects are believed to control most of the new properties observed in these artificial systems.[1] Despite the increasing progress in applications, a satisfactory microscopic knowledge of some fundamental physical aspects is still lacking. Paradigmatic is the case of the exchange interaction at the interface between an antiferromagnet (AFM) and a ferromagnet (FM),[2] which is used in most spintronic devices to pin (or stabilize) the magnetization of the adjacent thin FM film although there are still puzzles and experimental contradictions not well understood about its origin and effects.[2,3]

The interfacial exchange coupling in AFM/FM systems was discovered and initially described by Meiklejohn and Bean in 1956.[4] Experimentally, when an AFM/FM heterostructure is field cooled (FC) from above the Néel temperature (T_N) of the AFM layer,[2,4] and this undergoes the phase transition with the FM layer oriented in a certain direction,[5] an interfacial unidirectional anisotropy (K_E) is induced, which shifts the hysteresis loop away from zero field by the exchange bias field H_E. The naivest picture fails in predicting a value of H_E orders of magnitude larger than observed, or its vanishing at T_N (while it often occurs at a smaller temperature, referred as blocking temperature $T_B \leq T_N$.) The simple picture does not explain effects on the coercive field

J. M. Díez, J. L. F. Cuñado, R. Miranda, J. Camarero
Departamento de Física de la Materia Condensada and Instituto "Nicolás Cabrera"
Universidad Autónoma de Madrid
Madrid 28049, Spain
E-mail: julio.camarero@uam.es

P. Lapa, I. K. Schuller
Department of Physics and Center for Advanced Nanoscience
University of California
San Diego, La Jolla, CA 92093, USA

R. Solís, I. Arnay, P. Pedraz, P. Perna, A. Bollero
Instituto Madrileño de Estudios Avanzados en Nanociencia
IMDEA-Nanociencia
Campus Universidad Autónoma de Madrid
Madrid 28049, Spain

R. Miranda, J. Camarero
IFIMAC
Universidad Autónoma de Madrid
Madrid 28049, Spain

ADVANCED
SCIENCE NEWS
www.advancedsciencenews.com

ADVANCED
MATERIALS
INTERFACES
www.advmatinterfaces.de
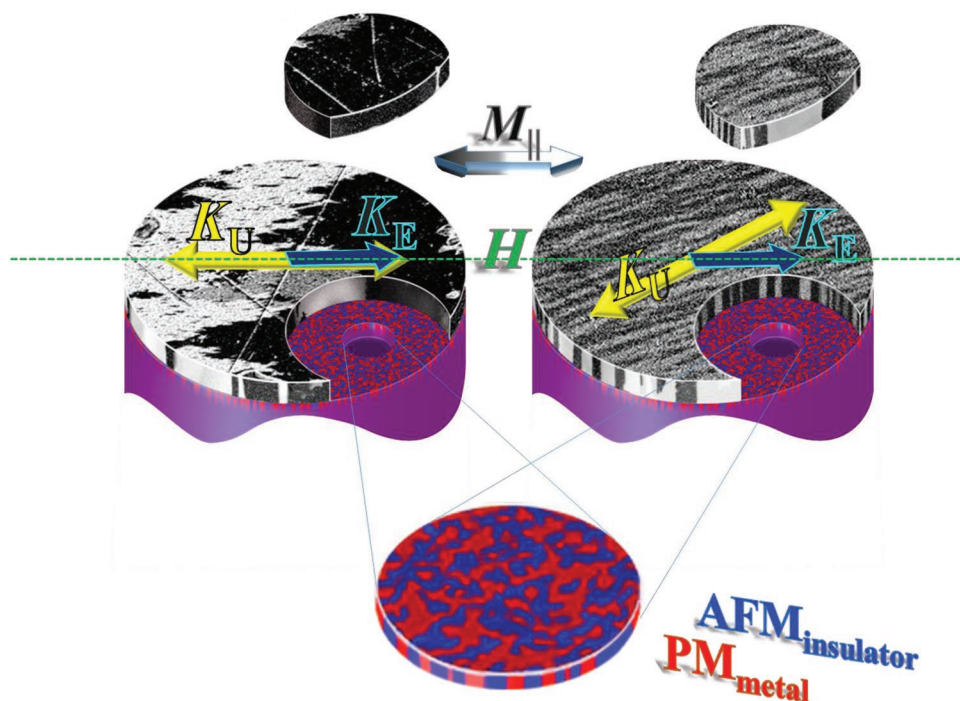
Figure 1. Illustration of the FM and AFM domain textures investigated: The relevant directions are indicated: uniaxial anisotropy of the FM layer K_U (yellow double arrow); interfacial unidirectional anisotropy (K_E (blue single arrow), which is aligned with the external in-plane magnetic field H (dashed green line). The directions are superimposed on representative Kerr microscopy images taken at room temperature during the magnetization reversal of the Co layer, with the external field applied along the direction of K_U (left image) and 50° away from it (right image), respectively. Field Cooling along those angle sets collinear and a non-collinear anisotropy configuration, respectively. The black to white color contrast indicates the orientation of the magnetization of the FM layer with respect to field direction, i.e., $M_\parallel$. The bottom image is a high-resolution co-localized near-field image showing the coexisting paramagnetic metallic (red) and antiferromagnetic insulating (blue) phases of the V_2O_3 layer during its phase transition.[27]

H_C, which is usually enhanced, nor possible asymmetries in the reversal of the FM layer. Many theoretical efforts have been made to predict the experimental observations,[6–12] mainly based on defects, thermal stabilities, and interfacial spin reorientations of both AFM and FM layers. Recent advances in magnetic-sensitive experimental techniques have thrown light on the underlying basic mechanisms at a given temperature that explain some of the observed properties.[13–22] Pinned and rotatable uncompensated AFM spins are claimed to be responsible for the reduced H_E[13] and the enhanced H_C.[14] The formation of domain wall structures on either side of the interface can also determine the magnitude of H_E,[15] and the intrinsic anisotropy of the FM layer has also a strong influence. The anisotropy ratio (K_E/K_U)[18,19] and the anisotropy configuration[20–22] seems to dictate the asymmetric reversal phenomena. This picture provides general fingerprints—non-negligible H_E, enhanced H_C, or reversal asymmetry—to disentangle at a given temperature the different exchange bias behaviors found in any AFM/FM system, including emerging molecular-based[23] and 2D-based[24] layered heterostructures. On the contrary, the general understanding of the temperature dependence of such fingerprints is still lack. For instance, further possible causes for the different behaviors of the exchange bias and coercive field as a function of temperature or for a reduced blocking temperature, even found for similar AFM/FM systems, are usually ascribed to intrinsic features of the AFM/FM system, such as interfacial defects, thicknesses, magnetic anisotropies, and AFM spin fluctuations.

In this study we show experimental evidence that provides new insights on the general knowledge about the phenomena of exchange bias and, surprisingly, refers to the key role of the magnetic texture of the FM layer during reversal, not considered to date. We have carried out temperature and angular-dependent magnetic and transport simultaneous measurements in an AFM/FM model system with tailored magnetic anisotropy configurations. The FM layer has a well-defined uniaxial anisotropy (K_U), while the interfacial unidirectional anisotropy K_E has been set by employing different Field Cooling (FC) angles (β_{FC}) during the first order Metal-Insulator Transition (MIT) of the AFM layer from a high temperature paramagnetic (PM) state. Thus, for exactly the same sample, collinear ($\beta_{FC} = 0°$) and non collinear ($\beta_{FC} = 50°$) configurations of the anisotropies have been set,[20,21] as schematically shown in **Figure 1**. At temperatures below, across, and above the MIT transition the magnetic behavior depends strongly on the anisotropy configuration. This shows that both the FM texture and magnetization reversal are responsible for the difference observed in exchange bias phenomena.

2. Results and Discussion

The sample consists in a FM, metallic Co layer with well-defined uniaxial anisotropy (K_U) deposited on top of a stoichiometric transition metal oxide V_2O_3 film. V_2O_3 is a canonical example

**ADVANCED
SCIENCE NEWS**
www.advancedsciencenews.com

**ADVANCED
MATERIALS
INTERFACES**
www.advmatinterfaces.de

of material which undergoes a first order Metal-Insulator Transition (MIT) at a critical temperature (T_{MIT} = 160 K, in bulk) with a change of several orders of magnitude in resistance, a simultaneous structural and magnetic phase transition, from a high temperature, rhombohedral, paramagnetic (PM) metal to a low temperature, monoclinic, antiferromagnetic (AFM) insulator.[25] A detailed description of the sample growth and microstructural characterization has been presented elsewhere,[26,28] and is summarized in the Experimental Section. The Co growth produces a layer with well-oriented terraces and voids ("rips") in the microstructure, which promote a well-defined uniaxial magnetic anisotropy, K_U, in the Co film at room temperature (RT),[28] when the V_2O_3 is a PM metal. The V_2O_3/Co sample is then field cooled (FC) well below T_{MIT} under an external magnetic field oriented at different directions with respect to K_U direction indicated by the β_{FC} angle, which fixes the direction of the interfacial unidirectional anisotropy (K_E). The magnetic and transport properties were simultaneously measured upon warming across the MIT transition after setting different anisotropy configurations.

Since at RT the V_2O_3 layer is paramagnetic, the intrinsic (growth-induced) anisotropy of the FM layer in the Co/V_2O_3 system can be obtained from vectorial-resolved magneto-optic Kerr effect (v-MOKE) measurements[29,30] (see Experimental Section). The left panels of **Figure 2** compare representative v-MOKE averaged hysteresis loops with the external in-plane field aligned (α_H = 0°) and misaligned (α_H = 50°) with respect to the rips direction. For α_H = 0°, the evolution of the in-plane magnetization components parallel ($M_\parallel$) and perpendicular ($M_\perp$) to the field direction indicate an easy axis (e.a.) behavior. The parallel component does not change from saturation M_S to remanence $M_{\parallel,R}$, i.e., $M_{\parallel,R}(0°)/M_S \approx 1$. For each field branch there is a single, sharp jump that reverts irreversibly the magnetization at the coercive field H_C (0°) = 6.3 mT. Additionally, $M_\perp(H) \approx 0$, indicating that the reversal takes place by nucleation and propagation of magnetic domains oriented parallel to the field direction which, in this case, coincides with the easy axis.

In clear contrast, for α_H = 50°, both $M_\parallel(H)$ and $M_\perp(H)$ loops display reversible (rounded) and irreversible (sharp) transitions, indicative of magnetization rotation and nucleation-propagation of magnetic domains, respectively.[31] In this case, the coercivity, i.e., the value at which $M_\parallel$ becomes zero, is smaller H_C (50°) = 4.6 mT, whereas $M_\perp \approx 0$ at a larger field (6.4 mT). For both angular conditions the descending and ascending field branches of the hysteresis loops are symmetric, and the irreversible transitions take place with the magnetization aligned near the anisotropy axis.

The central panel of Figure 2 displays the corresponding polar plots, i.e., $M_\parallel$ versus $M_\perp$, illustrating the very different reversal pathways of the magnetization vector for α_H = 0° and α_H = 50°. A detailed vectorial-resolved angular study focusing on the different reversal pathways found will be published elsewhere. In this representation, for each field branch, the data lying on the circle of radius unity represent reversible rotation
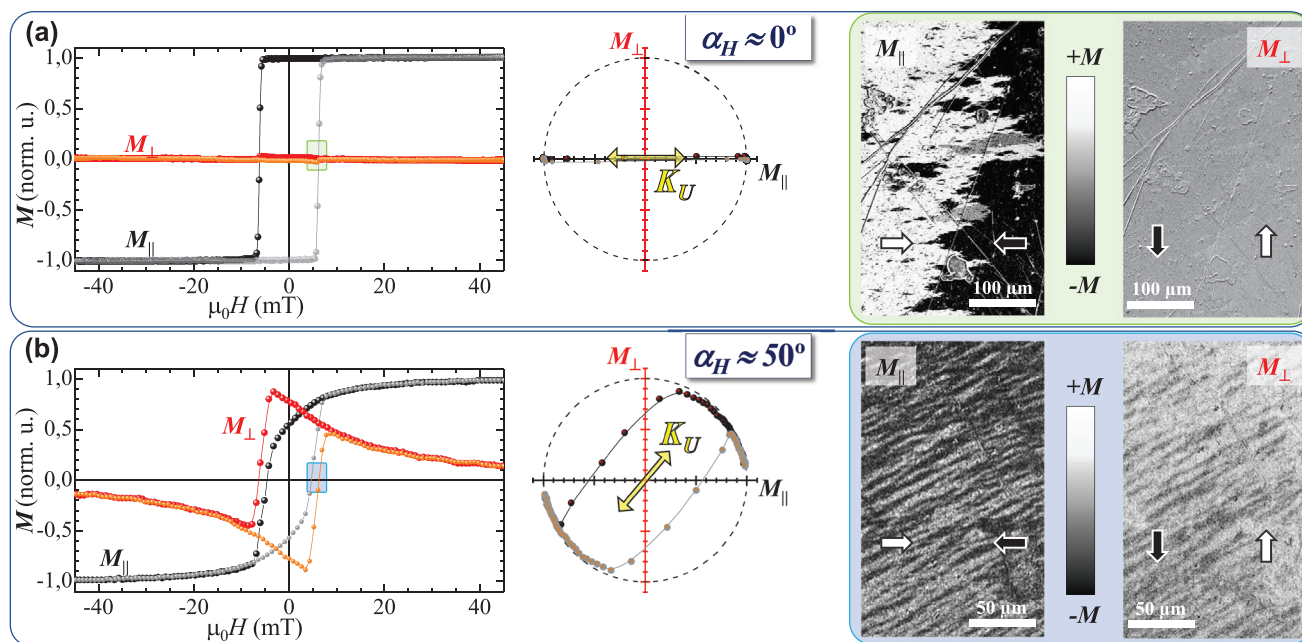
Figure 2. Room temperature magnetization reversal of the V_2O_3/Co sample at the indicated field angles α_H. At 300 K the V_2O_3 layer is paramagnetic, and the data reflect the intrinsic uniaxial magnetic anisotropy of the Co layer. a,b) Left panel: Standard representation of vectorial-resolved MOKE measurements, i.e., $M_\parallel(H)$ and $M\perp(H)$. The two branches of the hysteresis loop have been depicted with different filled symbols to clarify the evolution of the magnetization. Note the large difference in the reversal pathways for the two angular conditions. Central panel: Corresponding polar-plot representation, i.e., $M\perp$ ($M_\parallel$). The circle of radius unity depicted with a dashed line indicates the pure rotation of the magnetization vector, whereas the continuous lines are the corresponding simulated curves expected for a system with a well-defined uniaxial magnetic anisotropy K_U oriented along the direction of the rips. Right panel: v-MOKE microscopy magnetic images acquired during the reversal in the field region indicated by the boxes in (a) and (b). The left images are sensitive to the longitudinal $M_\parallel$ component, while the images at the right correspond to the transversal component ($M\perp$). For both angular conditions the magnetic domains are aligned with the anisotropy axis. Notice the orders of magnitude larger density of domains for α_H = 50°.

**ADVANCED
SCIENCE NEWS**
www.advancedsciencenews.com

**ADVANCED
MATERIALS
INTERFACES**
www.advmatinterfaces.de

processes.[31] Clearly, they are relevant for $\alpha_H = 50°$ and negligible for $\alpha_H = 0°$. In both cases, the paths connecting the points of departure and return to the circle are parallel to the anisotropy direction. This confirms that the nucleated magnetic domains are not oriented along the field direction, but rather along the easy axis direction. All the observed features are found every 180°, i.e., twofold magnetic symmetry, which is characteristic of a well-defined uniaxial magnetic anisotropy, K_U, oriented along the direction of the rips.

The right panels of Figure 2 display selected v-MOKE microscopy images recorded in the irreversible part of the hysteresis loops for the two angular conditions, which directly reveals the magnetic texture during the reversal.[31,32] The images at the left reflect the magnetization projected parallel to the field direction, i.e., $M_{\parallel}$, while the images at the right show the projection perpendicular to the field ($M_{\perp}$). Regions with black to white contrast indicate magnetic domains with opposite orientation. In general, the images show big domains, orders of magnitude larger than microstructure features which have slightly influence on both shape and dynamics of domain walls, as expected in well-defined (growth-induced) uniaxial anisotropy systems. The domain walls are not straight showing elongated structures at the microscale (≈ 10 μm wide), reminiscent of the special topography of the sample ($\approx$ tens of nanometer wide and several micrometer length features, see Figure S1, Supporting Information). The domain walls propagate according to the morphological pattern during reversal, and they do so more easily in the easy axis, i.e., when there are fewer domains and the front of the domain is much larger.

For $\alpha_H = 0°$ only two large domains (submillimeter size) are detected within the field of view, the $M_{\parallel}$-image displaying a large magnetic contrast, while almost no contrast is found in $M_{\perp}$-image. Remarkably, for $\alpha_H = 50°$ the number of domains (micrometer size) is two orders of magnitude larger, with a non-negligible contrast in both images, which is brighter in the $M_{\perp}$-image as expected from the corresponding averaged loop. This microscopic view of the hysteresis phenomena confirms that the irreversible transition consists in nucleation and propagation of magnetic domains oriented along K_U. Moreover, it reveals that propagative processes are more relevant when the field direction is aligned with the anisotropy axis, while nucleative ones become dominant when field and anisotropy axis are misaligned.

The interfacial anisotropy in the V$_2$O$_3$/Co bilayer is set after cooling the sample from RT to 50 K (i.e., well below $T_{MIT} = 160$ K) under an external in-plane magnetic field ($H_{FC} = +40$ mT). By using different FC directions (β_{FC}) with respect to the uniaxial anisotropy axis of the Co layer, collinear and non-collinear anisotropy configurations can be established on the same sample, as previously demonstrated in other AFM/FM systems.[20,21] The detailed vectorial-resolved angular study including both experimental and simulations with will be published elsewhere. This experimental procedure allows to study the temperature dependence of magnetic and transport properties for different, well-defined anisotropy configurations without any physical intervention (see Experimental Section).

Figure 3 compares the temperature evolution of the hysteresis loops after two selected positive-FC procedures corresponding to collinear ($\beta_{FC} = 0°$) and non-collinear ($\beta_{FC} = 50°$) anisotropy

configurations. The loops acquired at 50 K (top graphs of Figure 3) display similarities, hallmarks of interfacial exchange coupling phenomena,[7,19] and differences related to the set anisotropy configuration.[20,21] The loops are wider, horizontally shifted from zero field and opposite to the FC orientation, and asymmetric compared to the ones recorded at RT (bottom graphs). These features, i.e., enhanced coercivity, negative exchange bias and asymmetric magnetization reversal are fingerprints of interfacial exchange coupling effects taking place in the V$_2$O$_3$/Co bilayer, similarly to others AFM/FM bilayers.[14–24] Note that the non-collinear configuration (panel (b)) shows larger H_E and smaller H_C than the collinear one (panel (a)). The presence of AFM order in V$_2$O$_3$ at 50 K clearly promotes strong interfacial exchange coupling effect. Large coercivity enhancement below the transition has been already reported in similar V$_2$O$_3$/FM systems,[33–40] ascribed mainly to proximity effects during the transition, but the AFM order was not shown to induce strong exchange bias effects. In our case, the loops at low temperature show H_E/H_C ratio values ten times larger than previously reported,[38,39] ≈ 0.6 and 1 for collinear and non-collinear configuration, respectively. The derived interfacial exchange energy ($\sigma_E = H_E M_{Co} t_{Co} \approx 0.2$ and 0.4 mJ m^{-2}) is also substantially larger than reported before. The discrepancy might be due to an uncontrolled FC procedure and/or from a not well-defined anisotropy in the FM layer in previous studies. As the temperature increases, the evolution of the vectorial-resolved loops in Figure 3 provides a direct observation of the magnetic phase transition.[31] In general, the coercivity H_C decreases and the negative horizontal field shift from zero, i.e., the negative-Exchange Bias, decreases, vanishing at a given critical temperature, known as the Blocking Temperature T_B. Surprisingly, T_B depends strongly on the anisotropy configuration.

As the temperature increases, the evolution of the vectorial-resolved loops in Figure 3 provides a direct observation of the magnetic phase transition.[31] In general, the coercivity H_C decreases and the negative horizontal field shift from zero, i.e., the negative-Exchange Bias, decreases, vanishing at a given critical temperature, known as the Blocking Temperature T_B. Surprisingly, T_B depends strongly on the anisotropy configuration.

The loops in Figure 3 demonstrate that the magnetization reversal processes at low temperature are similar to those already found at RT, i.e., mostly governed by nucleation and propagation of domains for the collinear configuration ($\beta_{FC} = 0°$) and by rotational processes for the non-collinear one ($\beta_{FC} = 50°$). This is more evident with the vectorial analysis of magnetization reversal during warming (see Supporting Information[41]). Moreover, below the blocking temperature and for both anisotropy configurations, there is an asymmetric behavior in the decreasing and increasing field branches of the hysteresis loops (outlined graphs with colored background). The asymmetry is particularly evident in the $M_{\perp}(H)$ loops, where different maximum values of $M_{\perp}$ are observed for the two branches. The temperature at which the asymmetries disappear in $M_{\perp}$, i.e., T_B, depends on the initial anisotropy configuration and coincides with the onset of exchange bias, being 180 K for the collinear and 145 K for the non-collinear configuration, as discussed below.

Figure 4a–c compares the temperature evolution of the coercivity, (H_C), and the exchange bias (H_E) for the two selected
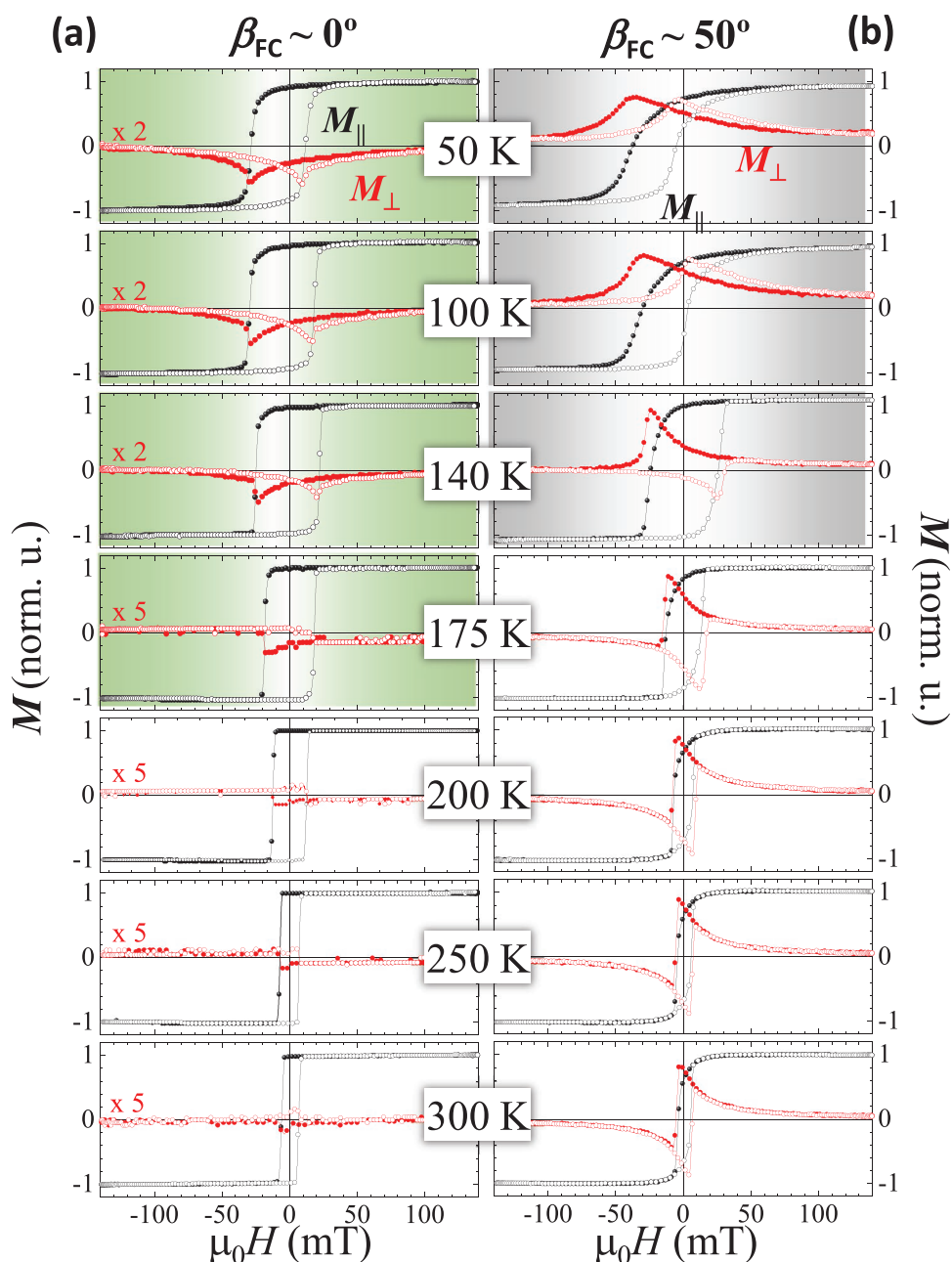
Figure 3. Temperature dependent v-MOKE hysteresis loops recorded after two selected positive-FC procedures on the same sample. a) Collinear ($\beta_{FC} \approx 0°$) anisotropy configuration; b) non-collinear ($\beta_{FC} \approx 50°$) configuration. $M_{\parallel}(H, T)$ and $M\perp(H, T)$ loops are represented by circles and squares, respectively. The descending (forward) and ascending (backward) field branches are depicted with filled (empty) symbols. Notice that in (a) there is exchange bias up to 180 K, whereas in (b) the exchange bias disappears above 140 K.

anisotropy configurations. For both configurations the exchange bias, H_E, is negative, i.e., opposite to the direction of magnetization of the FM layer during field cooling, and decreases with temperature. Figure 4c shows that below 120 K, H_E is twice as large for the non-collinear configuration than for the collinear one, while it vanishes at higher temperatures (180 K) for collinear ($\beta_{FC} \approx 0°$) than for non-collinear ($\beta_{FC} \approx 50°$) (145 K) arrangements of anisotropy. Moreover, the difference in the Blocking temperatures between the two configurations of the anisotropy is identical to the one deduced from the asymmetric

behaviour of the magnetization reversal (see Figure S3, Supporting Information[41]). Therefore, the onset of exchange bias and reversal asymmetry coincides, but it depends strongly on the anisotropy configuration, being ≈35 K higher for the collinear arrangement.

For both configurations, above the MIT ($T > 200$ K), the coercivity decreases with temperature, as expected from thermal activated effects, while well below the onset of the transition ($T < 130$ K) H_C increases only very slightly (≈5% in 100 K) with T. On the contrary, in the transition region (130 K < T > 200 K)
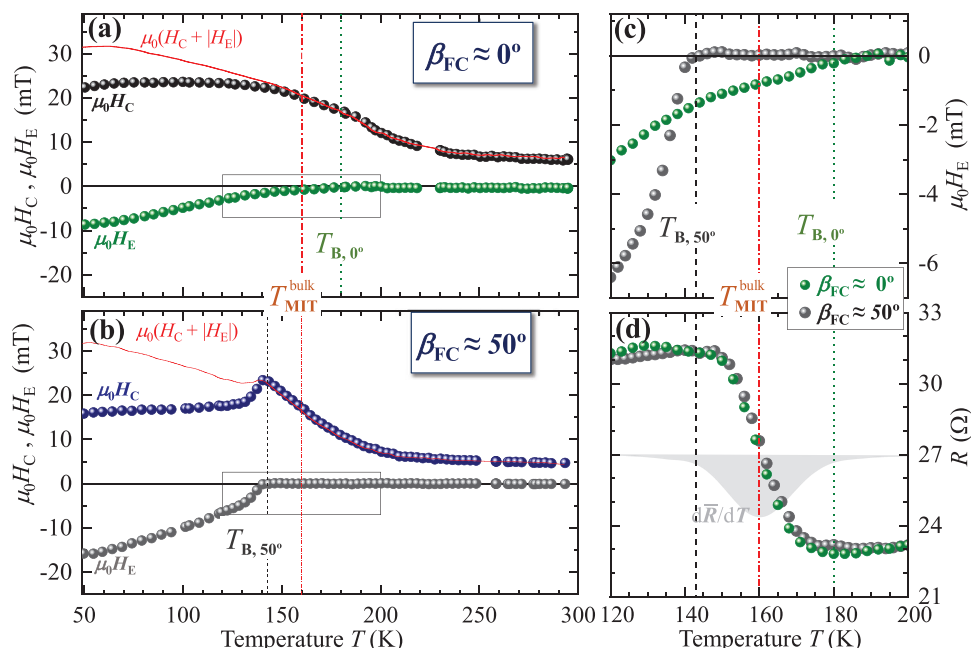
Figure 4. Temperature evolution of relevant magnetic and transport parameters after two FC procedures that produce a) collinear and b) non-collinear anisotropy configurations. c) Zoom of (a) and (b) around the MIT transition. d) Resistance (R) values for the two configurations. The values of coercivity ($\mu_0 H_C$) and exchange bias ($\mu_0 H_E$) have been extracted from in-plane hysteresis loops, such as the ones shown in Figure 3. The resistance (R) values are extracted from simultaneous conductivity measurements. The vertical lines correspond to the critical temperatures discussed in the text. Remarkably, both anisotropy configurations display similar resistance behaviour with temperature, whereas the relevant differences identified in the exchange bias phenomena originate from different reversal and FM textures.

and only for the non-collinear arrangement, the coercivity grows fast ($\approx 25\%$ in 12 K) and displays a maximum at 140 K, i.e., at the corresponding onset of H_E.

The large differences observed in the thermal evolutions of the magnetic properties for the two anisotropy configurations suggest a similar dependence on MIT and, consequently, different MIT transition temperature. On the contrary, simultaneous magnetic and transport measurements reveal a similar MIT transition for both β_{FC}, as shown in Figure 4. The MIT implies the coexistence of insulating AFM and metallic PM regions[27] in the V_2O_3 layer in a certain T range (≈ 40 K in this case), where nanotexture and size of the regions change. In our case, the use of the very same sample and the fixed warming sweep rate ensure similar size of domains in the V_2O_3 layer during the MIT transition[42] for both anisotropy configurations. In fact, the rate of change with temperature, i.e., dR/dT (T) (depicted with a shadowed area in Figure 4d, follows a single Gaussian, indicating that the distribution of transition temperatures is the same for both configurations. Note that the extreme values of the distribution match precisely the onsets of reversal asymmetry and exchange bias for $\beta_{FC} \approx 0°$ and $\beta_{FC} \approx 50°$, i.e., 145 and 180 K, respectively.

The experimental observations indicate that for the collinear configuration of the anisotropies the reversal of the FM layer is propagative, with large FM domains, the exchange bias after FC is small and the Blocking temperature is 180 K, i.e., at the high-T end of the MIT transition, when small and disconnected AFM regions are present in the V_2O_3 layer before becoming PM. On the contrary, for the non-collinear arrangement of the anisotropies, the reversal of the magnetization is nucleative,

with smaller FM domains and relevant rotation events. In this case the induced exchange bias is larger, and the Blocking temperature is 145 K, i.e., at the low-T beginning of the MIT transition, when larger and connected AFM regions are acting at the interface with the Co layer.

The physical picture rationalizing the large differences found in the temperature evolution of the magnetic properties relies on the different FM texture during reversal and similar MIT transition. The mean field theory explains the temperature range of the MIT transition whereas the random-field model addresses the different interfacial exchange-anisotropy effects for both anisotropy configurations.[8] The key point is that the size of the FM domains during reversal depends strongly on the field angle with respect to K_U direction, while the size of the AFM domains of the V_2O_3 layer does not, which is also a very fine domain structure, i.e., nanometer-sized (see bottom image of Figure 1). The random-field model predicts that the interfacial exchange energy ($\sigma_{FM/AFM}$) decreases statistically as $\sigma_{FM/AFM} \approx 1/\sqrt{N}$ with N being the number of AFM grains within one FM domain during reversal. Since the size of the FM domains is very large for the collinear arrangement ($\beta_{FC} \approx 0°$) (top left diagram of Figure 1), N is expected to be large and the exchange bias, smaller, in agreement with the experimental observations.

The peak observed for H_C in the non-collinear case around T_B can also be understood within this scenario. The weakening of K_E close to the transition allows a partial AFM spin reorientation dragged during FM reversal, thus, enhancing the coercivity. The effective drag will be favored by the small domains nucleated in the FM layer during the reversal process,

as Figure 3b shows. In the collinear case, on the contrary, K_E and K_U are aligned with the external field and the propagative reversal (see Figure 3a) does not favor AFM reorientation.

Similar arguments can be used to understand the different onset of H_E, i.e., different T_B, found for the non-collinear and collinear cases. Close to the magnetic transition, a weak interfacial exchange energy can promote either broadening (driven from the FM rotation dragging a similar AFM spin reorientation in both branches of the hysteresis loop) or a shift in the hysteresis loop (the collinearity and the propagative reversal hinder the AFM reorientation), respectively. This makes the depinning process more rapid for the non-collinear configuration, which eventually results in a lower blocking temperature. Note that the total interfacial exchange coupling effects, computed from $(H_C + | H_E |)$, behaves similarly in both anisotropy configurations (see Figure 4), which reflects the generality of the interface phenomenon, i.e., suggesting a similar landscape of uncompensated AFM spins, some fixed promoting the exchange bias and the rest rotatable boosting the coercive field, with different amounts depending of the anisotropy configuration and behaving in a different fashion below the blocking temperature.

It is worth to remark that, in general, there is a plethora of temperature evolutions reported for AFM/FM heterostructures, even for similar ones. In general, most of them show enhanced both exchange bias and coercivity at low temperature, which decrease as approaching the magnetic transition of the AFM layer, whereas in some specific cases there is a peak in the coercivity evolution close to this critical temperature. In turn, for identical AFM/FM systems is expected similar T_B values. Our results reflect different behaviors in the same sample, ruling out any influence related to defects or thicknesses, via engineering the magnetic anisotropy configuration in a control way, which in addition modifies T_B, and everything can be understood considering the magnetic texture of the FM layer during reversal.

3. Conclusion

In summary, our results show a new general mechanism controlling the exchange bias phenomena in AFM/FM systems. The magnetic texture of the FM layer in the heterostructure has a strong influence in the interfacial EB effects including reversal pathways, H_E, H_C, and T_B and their temperature dependences. This is done by using a well-defined V_2O_3/Co model system in which the anisotropy of the FM layer and the interface anisotropy, established during field cooling, are set in controlled configurations without changing the structure of the sample, and measuring magnetic and transport properties simultaneously. The ferromagnetic Co layer has an (growth) induced well-defined uniaxial magnetic anisotropy, whereas the V_2O_3 layer undergoes a first-order phase transition with nanotextured phase coexistence of paramagnetic-metal and antiferromagnetic-insulator phases, which allows tracking magnetic and transport characteristics. While the transport properties for the two anisotropy configurations do not differ, the collinear arrangement results in smaller exchange bias H_E and higher T_B.

Furthermore, the discovery of the mechanism described here allows us to tailor the aforementioned EB phenomena, which gave us the chance to investigate long standing open questions. The large differences found in similar AFM/FM systems regarding the temperature evolution of important magnetic parameters (e.g., exchange bias, coercivity enhancement, and reduced blocking temperature) as well as reversal processes (including asymmetries) have been found in the very same sample, ruling out any influence related to defects or thicknesses. With this discovery, EB phenomena can be controlled microscopically, which results in an unprecedented opportunity not only to study local interactions, but to enhance the capabilities of existing devices relying on Exchange Bias and to design innovative ones that were simply not possible before.

Our results provide a general microscopic view that can be extended to any AFM/FM system[42–45] and should encourage new models to be developed, which don't pay attention to the texture of the FM layer. Secondly, exchange-bias phenomena are at the heart of spintronics applications, either to provide magnetic stability or to provide new functionalities. Therefore, the key role of the intrinsic FM texture during reversal could be used to design interfacial effects at will, i.e., tailored reversal pathways or T_B with enhanced H_E and H_C, which can be combined with spin-orbit-torque driven exchange bias manipulation,[46,47] opening new paths to develop future spintronic devices.

4. Experimental Section

V_2O_3 (100 nm)/Co (15 nm) bilayers were grown in a high vacuum chamber ($P_{Base} < 10^{-5}$ Pa) on r-cut (102) sapphire α-Al_2O_3. The r-cut (102) sapphire substrate was chosen because V_2O_3 film grown on it present the largest and sharpest MIT.[34] The V_2O_3 film was grown from a stoichiometric target by RF magnetron sputtering, power was kept at 100 W and the total Ar pressure was 4 mT with the substrate kept at 1000 K. A detailed account of the V_2O_3 deposition and characterization can be found elsewhere.[27,28] Co was then deposited at 300 K by e-beam evaporation. The coincidence of the metal-insulator (proven by transport measurements) and the structural phase transitions (proven by XRD) was checked.[26] The V_2O_3/Co surface microstructure obtained from atomic force microscopy and scanning electron microscopy reveals extended rips and localized voids oriented along the V_2O_3 (015) diffraction vector, emphasized by the ellipsoidal shape of the corresponding Fourier transform images (see Figure S1, Supporting Information). The rips and voids promoting the uniaxial magnetic anisotropy in the FM layer are ≈tens of nanometer in width, with length ranging from 80 nm to several hundred nanometers (>500 nm on average).

All measurements were performed after cooling the sample from RT to 50 K under an external in-plane magnetic field (H_{FC} = +40 mT) oriented at different angles (β_{FC}) with respect to K_U direction.[23] This allowed to control the magnetization direction of the FM layer across the metal-insulator transition during cooling and, importantly, to set the interfacial exchange anisotropy K_E at different angles with respect to K_U axis. The collinear (non-collinear) anisotropy configuration was achieved by aligning (misaligning) β_{FC} with respect to K_U direction.[18,19]

Averaged v-MOKE and four-point current in-plane measurements were acquired simultaneously, without changing the angle of the field (i.e., $\alpha_H = \beta_{FC}$), during warming of the sample from 50 K to RT. Training effects were not considered since the signal was averaged over many hysteresis loops by using a 3.1 Hz triangular magnetic field ramp. At a given temperature, a simple inspection of the in-plane vectorial magnetization loops provides direct information on the magnetization reversal processes, highlighting the importance of v-MOKE. In general,

hysteresis loops show sharp (irreversible) and smooth (reversible) magnetic transitions in both components (e.g., see Figure 2, Figure 3, and Figure S2, Supporting Information). The different pathways are more evident for the $M_\perp H$ loop. The irreversible transitions correspond to nucleation and further domain wall propagation (see right panels of Figure 2) whereas the reversible ones are associated to magnetization rotation processes (see vectorial representation of the hysteresis curves, i.e., $M_\parallel$ ($M_\perp$), of Figure 2 and Figure S2, Supporting Information). The relative weight of these two reversal mechanisms depends on T and β_{FC}, as discussed in the text. Since the structural and electronic configuration of the V_2O_3 film crucially depends on the temperature, a similar (slow) temperature sweep rate ($\approx$1.5 K min^{-1}) was used in all measurements, to minimize any temperature scanning rate dependence.[48] v-MOKE measurements were carried out at the same applied field sweep rate, to avoid having to consider dynamical effects due to the applied field sweep rate.[49] Note that this experimental procedure allows to carry out transport and magnetic characterization at different temperatures with different tailored anisotropy configurations without any physical intervention.

Relevant magnetic parameters such as coercivity (H_C), exchange bias (H_E), and asymmetry (ζ) have been obtained from the loops. H_C refers to the magnetic field required to reduce to zero the magnetization parallel to the field, i.e., $M_\parallel(H_C) = 0$, and it is averaged from the forward (descending) and backward (ascending) field branch (see Figure 3), i.e., $H_C = 1/2$ ($H_C^{back} - H_C^{forw}$). Note that the coercive field in each branch coincides with the maximum of the $M_\perp(H)$ loop,[17] so finally the average value from both magnetization loops was obtained. H_E refers to the horizontal shift of the hysteresis loop, i.e., $H_E = 1/2$ ($H_C^{back} + H_C^{forw}$). ζ values are derived from the maximum values of the descending (forward) and ascending (backward) field branch of the $M_\perp(H)$ loops (see Figure S3, Supporting Information).

Supporting Information

Supporting Information is available from the Wiley Online Library or from the author.

Acknowledgements

Conflict of Interest

The authors declare no conflict of interest.

Data Availability Statement

The data that support the findings of this study are available from the corresponding author upon reasonable request.

[1] F. Hellman, A. Hoffmann, Y. Tserkovnyak, G. S. Beach, E. E. Fullerton, C. Leighton, A. H. MacDonald, D. C. Ralph, D. A. Arena, H. A. Dürr, P. Fischer, *Rev. Mod. Phys.* **2017**, *89*, 025006.

[2] a) J. Nogués, I. K. Schuller, *J. Magn. Magn. Mater.* **1999**, *192*, 203; b) A. E. Berkowitz, K. Takano, *J. Magn. Magn. Mater.* **1999**, *200*, 552.

[3] F. Radu, H. Zabel, *Exchange Bias Effect of Ferro-/Antiferromagnetic Heterostructures*, Springer, Berlin, Heidelberg, **2008**, p. 97.

[4] W. H. Meiklejohn, C. P. Bean, *Phys. Rev.* **1956**, *102*, 1413.

[5] A. Migliorini, B. Kuerbanjiang, T. Huminiuc, D. Kepaptsoglou, M. Muñoz, J. L. F. Cuñado, J. Camarero, C. Aroca, G. Vallejo-Fernández, V. K. Lazarov, J. L. Prieto, *Nat. Mater.* **2018**, *17*, 28.

[6] L. Neel, *Ann. Phys.* **1967**, *2*, 61.

[7] D. Mauri, H. C. Siegmann, P. S. Bagus, E. Kay, *J. Appl. Phys.* **1987**, *62*, 3047.

[8] A. P. Malozemoff, *Phys. Rev. B: Rapid Commun.* **1987**, *35*, 3679.

[9] K. Kiwi, *J. Magn. Magn. Mater.* **2001**, *234*, 584.

[10] U. Nowak, K. D. Usadel, J. Keller, P. Milt'enyi, B. Beschoten, G. Güntherodt, *Phys. Rev. B* **2002**, *66*, 014430.

[11] J. V. Kim, R. L. Stamps, *Phys. Rev. B* **2005**, *71*, 094405.

[12] F. Radu, A. Westphalen, K. Theis-Bröhl, H. Zabel, *J. Phys.: Condens. Matter* **2006**, *18*, L29.

[13] H. Ohldag, A. Scholl, F. Nolting, E. Arenholz, S. Maat, A. T. Young, M. Carey, J. Stöhr, *Phys. Rev. Lett.* **2003**, *91*, 017203.

[14] J. Camarero, Y. Pennec, J. Vogel, S. Pizzini, M. Cartier, F. Fettar, F. Ernult, A. Tagliaferri, N. B. Brookes, B. Dieny, *Phys. Rev. B* **2003**, *67*, 020413R.

[15] J. Camarero, Y. Pennec, J. Vogel, M. Bonfim, S. Pizzini, F. Fettar, F. Ernult, F. Garcia, F. Lançon, L. Billard, B. Dieny, A. Tagliaferri, N. B. Brookes, *Phys. Rev. Lett.* **2003**, *91*, 027201.

[16] A. Hoffmann, M. Grimsditch, J. E. Pearson, J. Nogués, W. A. D. A. Macedo, I. K. Schuller, *Phys. Rev. B* **2003**, *67*, 220406.

[17] J. Camarero, J. Sort, A. Hoffmann, J. M. García-Martín, B. Dieny, R. Miranda, J. Nogués, *Phys. Rev. Lett.* **2005**, *95*, 057204.

[18] J. Camarero, J. Miguel, J. Goedkoop, J. Vogel, F. García, F. Romanens, S. Pizzini, N. B. Brookes, J. Sort, B. Dieny, *Appl. Phys. Lett.* **2006**, *89*, 232507.

[19] E. Jiménez, J. Camarero, J. Sort, J. Nogués, A. Hoffmann, N. Mikuszeit, J. M. García-Martín, B. Dieny, R. Miranda, *Phys. Rev. B* **2009**, *80*, 014415.

[20] E. Jiménez, J. Camarero, J. Sort, J. Nogués, A. Hoffmann, F. J. Teran, P. Perna, J. M. García-Martín, B. Dieny, R Miranda, *Appl. Phys. Lett.* **2009**, *95*, 122508.

[21] E. Jiménez, J. Camarero, J. Sort, J. Nogués, A. Hoffmann, N. Mikuszeit, P. Perna, B. Dieny, R. Miranda, *J. Appl. Phys.* **2011**, *109*, 07D730.

[22] R. Morales, A. C. Basaran, J. E. Villegas, D. Navas, N. Soriano, B. Mora, C. Redondo, X. Batlle, X. Schuller, *Phys. Rev. Lett.* **2015**, *114*, 097202.

[23] J. Jo, I. Byun, I. Oh, J. Park, M. J. Jin, B. C. Min, J. Lee, J. W. Yoo, *ACS Nano* **2018**, *13*, 894.

[24] G. Hu, Y. Zhu, J. Xiang, T. Y. Yang, M. Huang, Z. Wang, P. Liu, Y. Zhang, C. Feng, D. Hou, *ACS Nano* **2020**, *14*, 12037.

**ADVANCED
SCIENCE NEWS**

www.advancedsciencenews.com

**ADVANCED
MATERIALS
INTERFACES**

www.advmatinterfaces.de

[25] M. Imada, A. Fujimori, Y. Tokura, *Rev. Mod. Phys.* **1998**, *70*, 1039.

[26] T. Saerbeck, J. de la Venta, S. Wang, J. G. Ramirez, M. Erekhinky, I. Valmianski, I. K. Schuller, *J. Mater. Res.* **2014**, *29*, 2353.

[27] A. S. McLeod, E. V. Heumen, J. G. Ramirez, S. Wang, T. Saerbeck, S. Guenon, M. Anderegg, Goldflam, P. Kelly, A. Mueller, K. Liu, I. K. Schuller, D. N. Basov, *Nat. Phys.* **2016**, *13*, 80.

[28] D. A. Gilbert, J. G. Ramírez, T. Saerbeck, J. Trastoy, I. K. Schuller, K. Liu, J. de la Venta, *Sci. Rep.* **2017**, *7*, 13471.

[29] E. Jiménez, N. Mikuszeit, J. L. F. Cuñado, P. Perna, J. Pedrosa, D. Maccariello, C. Rodrigo, M. A. Niño, A. Bollero, J. Camarero, R. Miranda, *Rev. Sci. Instrum.* **2014**, *85*, 053904.

[30] J. L. F. Cuñado, J. Pedrosa, F. Ajejas, A. Bollero, P. Perna, F. J. Teran, J. Camarero, *Rev. Sci. Instrum.* **2015**, *86*, 046109.

[31] J. L. F. Cuñado, J. Pedrosa, F. Ajejas, A. Bollero, P. Perna, R. Miranda, J. Camarero, *J. Phys.: Condens. Matter* **2017**, *29*, 405805.

[32] A. Hubert, R. Schäfer, *Magnetic Domains: The Analysis of Magnetic Microstructures*, Springer Science and Business Media, **2008**.

[33] Y. Kalcheim, N. Butakov, N. M. Vargas, M. H. Lee, J. del Valle, J. Trastoy, P. Salev, P. Schuller, I. K. Schuller, *Phys. Rev. Lett.* **2019**, *122*, 057601.

[34] M. I. Montero, K. Liu, O. M. Stoll, A. Hoffmann, J. J. Akerman, J. I. Martín, J. L. Vicent, S. M. Baker, T. P. Russell, C. Leighton, *J. Phys. D: Appl. Phys.* **2002**, *35*, 2398.

[35] I. Valmianski, J. G. Ramírez, C. Urban, X. Batlle, I. K. Schuller, *Phys. Rev. B* **2017**, *95*, 155132.

[36] J. De La Venta, S. Wang, J. G. Ramírez, I. K. Schuller, *Appl. Phys. Lett.* **2013**, *102*, 122404.

[37] J. De La Venta, S. Wang, T. Saerbeck, J. G. Ramírez, I. Valmianski, I. K. Schuller, *Appl. Phys. Lett.* **2014**, *104*, 062410.

[38] B. Sass, C. Tusche, W. Felsch, F. Bertran, F. Fortuna, P. Ohresser, G. Krill, *Phys. Rev. B* **2005**, *71*, 014415.

[39] B. Sass, S. Buschhorn, W. Felsch, D. Schmitz, P. Imperia, *J. Magn. Magn. Mater.* **2006**, *303*, 167.

[40] J. Trastoy, Y. Kalcheim, J. del Valle, I. Valmianski, I. K. Schuller, *J. Mater. Sci.* **2018**, *53*, 9131.

[41] See supplementary material at .... for the details about the vectorial analysis of the temperature dependence of magnetization reversal and the comparison of the evolution of asymmetry and exchange bias during the warming for the studied configurations.

[42] P. H. Lin, B. Y. Yang, M. H. Tsai, P. C. Chen, K. F. Huang, H. H. Lin, C. H. Lai, *Nat. Mater.* **2019**, *18*, 335.

[43] T. Jungwirth, J. Sinova, A. Manchon, X. Marti, J. Wunderlich, C. Felser, *Nat. Phys.* **2018**, *14*, 200.

[44] J. Huang, H. Wang, X. Wang, X. Gao, J. Liu, H. Wang, *ACS Appl. Mater. Interfaces* **2020**, *12*, 39920.

[45] Y. L. Huang, D. Nikonov, C. Addiego, R. V. Chopdekar, B. Prasad, L. Zhang, J. Chatterjee, H. J. Liu, A. Farhan, Y. H. Chu, M. Yang, *Nat. Commun.* **2020**, *11*, 1.

[46] P. H. Lin, B. Y. Yang, M. H. Tsai, P. C. Chen, K. F. Huang, H. H. Linn, C. H. Lai, *Nat. Mater.* **2019**, *18*, 335.

[47] S. Peng, D. Zhu, W. Li, H. Wu, A. J. Grutter, D. A. Gilbert, J. Lu, D. Xiong, W. Cai, P. Shafer, K.L Wang, *Nat. Electron.* **2020**, *3*, 757.

[48] T. Bar, S. K. Choudhary, A. Ashraf, K. S. Sujith, S. Puri, S. Raj, B. Bansal, *Phys. Rev. Lett.* **2018**, *121*, 045701.

[49] J. L. F. Cuñado, A. Bollero, T. Pérez-Castañeda, P. Perna, F. Ajejas, J. Pedrosa, A. Gudín, A. Maldonado, M. A. Niño, R. Guerrero, D. Cabrera, F. J. Terán, R. Miranda, J. Camarero, *Sci. Rep.* **2017**, *7*, 13474.